Simultaneous measurement of axial strain and temperature based on a twin-core single-hole fiber with the optical Vernier effect

YUJIAN LI, Ⓘ YIFAN LIU, WEIHAO YUAN, Ⓘ AND CHANGYUAN YU* Ⓘ

Photonics Research Institute, the Department of Electronic and Information Engineering, The Hong Kong Polytechnic University, Hong Kong, China
*changyuan.yu@polyu.edu.hk

Abstract: An ultrasensitive optical fiber sensor based on the optical Vernier effect is proposed for the simultaneous measurement of axial strain and temperature. The sensor structure comprises two cascaded Mach-Zehnder interferometers (MZIs) with different free space ranges. The single MZI is built up by fusion splicing a segment of ~3 mm twin-core single-hole fiber (TCSHF) between two pieces of ~5 mm none core fibers (NCF). When acting separately, each MZI can respond linearly to the axial strain change with a sensitivity of ~ 0.6 pm/με and temperature with a sensitivity of ~34 pm/°C. When the two MZIs are cascaded in series, the sensitivities are amplified about 30 times because of the optical Vernier effect. Experimental results demonstrate that the cascaded structure exhibits a high axial strain sensitivity of ~ 17 pm/με in the range of 0 to 2000 με and temperature sensitivity of ~1.16 nm/°C in the range of 30 to 70 °C. Moreover, the cascaded structure can simultaneously measure the axial strain and temperature change in the acceptable error ranges.

1. Introduction

Optical fiber sensors have been widely applied in vital sign acquisition [1], structural health analysis, environmental monitoring, and many other engineering measurement fields on account of their unique characteristics, including compact structure, high sensitivity, durability in the long term, anti-electromagnetic interference, and so on [2–5].

Axial strain is one of optical fiber sensors' commonly measured physical parameters. Up to now, researchers have proposed many structures and technologies based on single-mode fiber (SMF). For example, different types of fiber grating, including fiber Bragg grating (FBG) [6], long-period fiber grating (LPFG) [7], long helical period fiber grating (HLPFG) [8], and tilted fiber Bragg grating (TFBG) [9] are inscribed in SMFs because the grating period changes with the applied axial strain. Many SMF-based secondary machining structures, including but not limited to taper [10], offset [11], and S- or Z-shaped structures [12–14], are designed and fabricated with the expectation of higher sensitivity. In addition, several axial strain sensors based on special microstructure fibers are gradually emerging with the development of fiber drawing technology. Hollow-core fiber (HCF) [15], polarization-maintaining fiber (PMF) [16], and twin-core photonic crystal fiber (TCPCF) [17] are some examples. However, such axial strain sensors' sensitivities are relatively low, always under 10 pm/με [18].

An effective way to enhance the sensitivity of the optical fiber sensors is by building a cascaded interference structure based on the Optical Vernier effect [19]. When two interferometers with similar free spectral ranges (FSR) are combined, an envelope is introduced on the final spectrum because of the optical Vernier effect. Supposing one of the interferometers' spectrums has a small amount of drift, the envelope of the superimposed spectrum will also have several times the amount of drift, which amplifies the sensitivity by orders [20].

The availability of the optical Vernier effect has been experimentally demonstrated on different kinds of interferometric structures, such as the Sagnac interferometer (SI) [21], Fabry-Perot interferometer (FPI) [22], Michelson interferometer (MI) [23], Mach-Zehnder interferometer (MZI) [24], hybrid-type configurations [25], etc. It is unsuitable for measuring the axial strain change along one dimension for optical fiber SI because of the fiber ring. For optical fiber FPI, the common structures are fusion splicing SMF with HCF [26], splicing fusion SMF based on offset structure [27], or etching an air cavity by laser [28]. The cavity length of the FPI is about 50 μm which needs a relatively high precision control process. Thus, FPI sensors with good repeatability are challenging to obtain. Two MIs cascaded structures are rarely reported because their complex sensing structures are difficult to be built up. The hybrid-type configuration is built up by combining different types of interferometers, which are always associated with complicated structures and complex fabrication processes. For MZI, the sensing mechanism is easy to achieve, and the fabrication process does not need high precision because its size is always at the level of ~5 mm.

The first demonstration of using MZIs based on the Optical Vernier effect was reported by Liao et al. in 2017 [24]. In their work, two traditional MZIs with two light arms are connected in series by 3 dB couplers to measure curvature and temperature. Then, Wang et al. proposed a parallel configuration based on two MZIs separated by two 3 dB couplers in 2019 [29]. The other type of MZIs-based sensor is built up by fabricating the two interferometers in the fiber, which do not need any other connected devices. Compared to the aforementioned two structures, the size of the all-fiber design is much smaller, which is helpful in integrated systems. In addition, the sensitivity of the third type of sensor is much higher than the other two types [30].

In this paper, a cascaded MZIs sensor based on the optical Vernier effect is designed and fabricated to simultaneously measure axial strain and temperature. Every MZI is built based on the twin-core single-hole fiber (TCSHF). Since the construction method of the MZI is quite simple and does not need high precision, the repeatability of the fabrication process can be guaranteed. By optimizing the fusion splicing parameters, the fusion collapse is avoided, and then an MZI with good robustness is achieved. After two MZIs are cascaded together, the sensor can measure the axial strain with a sensitivity of ~ 17 pm/με from 0 to 2000 με and temperature with a sensitivity of ~1.16 nm/°C from 30 to 70 °C. The sensitivities are much higher than the common MZIs proposed before. Moreover, the cascaded structure can simultaneously detect the axial strain and temperature change in the acceptable error range.

2. Sensor structure and fabrication

2.1. Mach-Zehnder interferometer

As shown in Fig. 1, a short section of TCSHF is fusion spliced between two short pieces of None core fiber (NCF). The function of the NCF is quite the same as that of the optical coupler. It can not only enlarge the mold field so that the input light can be divided evenly into the different transmitted channels of the TCSHF but also can couple the light from different channels together so that the final output light can propagate in SMF. The two cores and the air hole of the TCSHF create the possibility of building up an MZI.

2.2. None core fiber

The length of NCF determines the mode field distribution at the NCF-TCSHF fusion splicing point, which also influences the mode field distribution along the TCSHF. Thus, a simulation experiment is conducted to find out the proper length of NCF. Considering the circular symmetry of the SMF and NCF, a 2D model of the SMF-NCF structure is built up, as shown in Fig. 2(a). The length of the SMF is 5 mm, and the effective refractive index (EFI) of the core and cladding is 1.4504 and 1.4447, respectively. The size of the NCF is 20 mm, and its EFI is 1.4575. Figure 2(b)
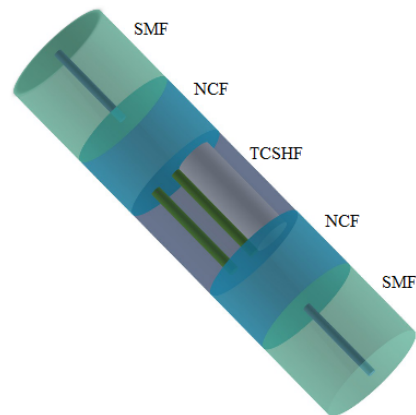
Fig. 1. The schematic diagram of the MZI structure is based on NCF and TCSHF.

shows the mode field distribution in the SMF-NCF structure. It can be seen that there will be many autofocus points along the direction of light transmissions, such as the trisection autofocus points at the position of ~5 mm NCF, the halving autofocus points at the position of ~7.5 mm NCF, and the entire autofocus point at the position of ~15 mm NCF.
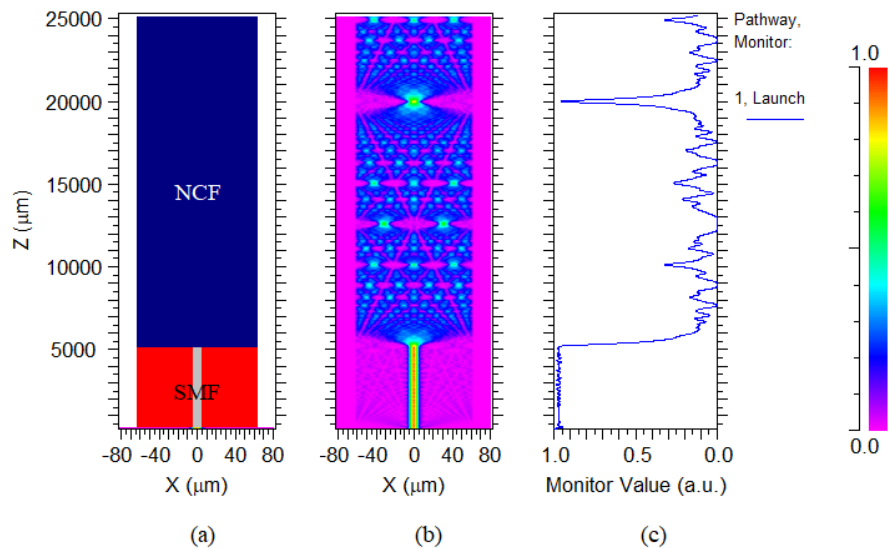

Fig. 2. (a) The 2D model of the SMF-NCF structure; (b) The mode field distribution in the SMF-NCF structure; (c) The intensity of the transmission light in the SMF-NCF structure.

For building up a Mach-Zehnder interferometer in TCSHF, the distribution of the light field should be as even as possible at the NCF-TCSHF fusion splicing point. Thus, the length of the halving autofocus points (~7.5 mm) and the entire autofocus point (~15 mm)cannot help achieve the objective. Finally, taking the final size of the sensor and the cutting precision of the optical fiber cleaver (Sumitomo Electric Industries, Ltd., FC-6S) into account, the final length of the NCF is determined as 5 mm.

2.3. Twin-core single-hole fiber

The TCSHF used in this work is designed and fabricated by Yangtze Optical Electronic Co., Ltd. From Fig. 3(a), the cross-section of the TCSHF can be seen clearly. Two cores (core A and core B) and an air hole are distributed in the fiber. Core A is away from the central point at a distance of ~25 μm, and its diameter is ~9.8 μm. With the same diameter, core B is at the central position of the fiber. The air hole is also off-center distributing with a distance of ~27 μm, and its diameter is ~42.2 μm. The center points of the two cores and the air hole are on the same line, as shown in Fig. 3. The refractive index of the two cores' material is 1.4625@630 nm, and the refractive index of the cladding material is 1.4575@630 nm.
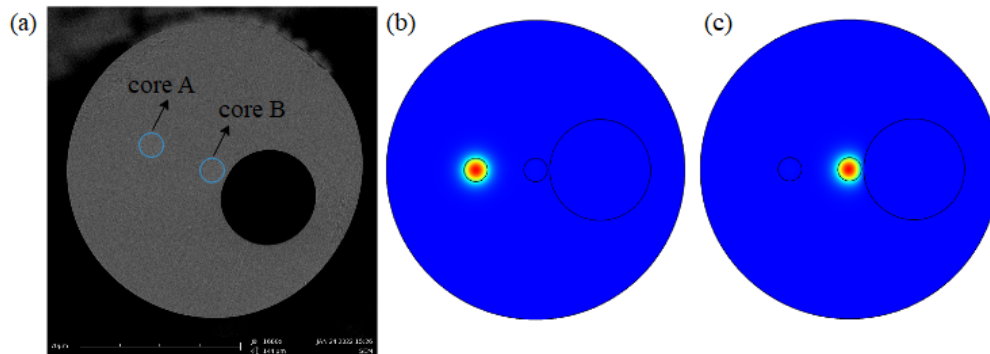

Fig. 3. (a) The cross-section of the TCSHF under an electron microscope; (b) The fundamental mode at core A; (c) The fundamental mode at core B.

Figure 3(b) and Fig. 3(c) display simulation results of the fundamental mode distribution in the TCSHF. The simulation wavelength is 1550 nm. Different from the uniform distribution of the mode field in core A, the mode field distribution in core B is off the center point and away from the air hole. The EFI of the fundamental mode in cores A and B is 1.460148 and 1.460009, respectively.

Since there is a big air hole in the TCSHF, a collapse will appear when TCSHF is spliced with other fiber types. Several splicing fusion experiments were conducted to find out the most proper splicing fusion parameters, which can help avoid this undesirable collapse feature. The final optimum fusion parameters are shown in Table 1.

Table 1. The optimum fusion parameters between TCSHF and NCF

Parameters	Value
The intensity of clean discharge	30
Time of clean discharge	100 ms
The intensity of the first discharge	90
Time of the first discharge	300 ms
The intensity of the second discharge	20
Time of the second discharge	200 ms
Pre-melting time	100 ms
Splicing fusion front end interval	20 μm
The propulsion distance along the Z-axis	15 μm
The type of alignment	cladding

Figure 4 displays the fusion splicing point between NCF and TCSHF based on the parameters in Table 1. The boundary between the two types of fiber is distinct, and the collapse phenomenon did not happen as expected.

Fig. 4. The microscope image of the fusion splicing point between NCF and TCSHF.

The NCF-TCSHF-NCF sandwich structures with different lengths of the TCSHF are experimentally fabricated in this work. As shown in Fig. 5. the final transmission spectrum contains an envelope curve and a cosine curve. In this work, the sensing characteristic of the envelope curve is not used and discussed. As the length increases, the period of the cosine curve gets smaller. According to the theory of MZ interference, the FSR can be calculated by the following equation.

$$FSR = \Delta\lambda = \frac{\lambda_1\lambda_2}{\Delta nL} \approx \frac{\lambda^2}{\Delta nL}. \tag{1}$$

Where λ is the wavelength interference dip, L is the length of the TCSHF, and Δn is the difference in the effective refractive index. Take 3 mm TCSHF as an example. The FSR is 1.86 nm, and the Δn can be calculated as 0.423 according to (1). Thus, one of the two light beams involved in the MZ interference is transmitting in the air hole, and the other is in the fiber core. For convenience, this sensor is marked as Sensor 1 in the following discussion.

To figure out whether the length of NCF can influence the final spectrum, a comparative experiment is conducted by fabricating a new sensor with different fabrication parameters. The length of NCF and TCSHF in this sensor structure is 2 mm and 3 mm, respectively. The transmitted spectrum is shown in Fig. 6 by the blue line, and the FSR of this sensor is ~1.86 nm. Thus, it can be inferred that the length of NCF does not influence the FSR of the MZI, and the FSR of the MZI is only determined by the length of TCSHF. Once again, it is demonstrated that the MZ interference only occurs in the TCSHF. Finally, taking the final size of the sensor and the complexity of preparation into account, the final length of the TCSHF is determined as 3 mm. Another sensor with the same fabrication parameters as Sensor 1 is fabricated to test the repeatability of the proposed TCSHF sensor and its spectrum is shown in Fig. 6 by a red line. This sensor is marked as Sensor 2, and the FSR is ~1.92 nm. The FSR difference between the two sensors is 0.08 nm, which is in the range of the errors permitted because the cutting precision of the optical fiber cleaver is 1 mm. Thus, the preparation repeatability of the proposed MZI sensor is quite good.
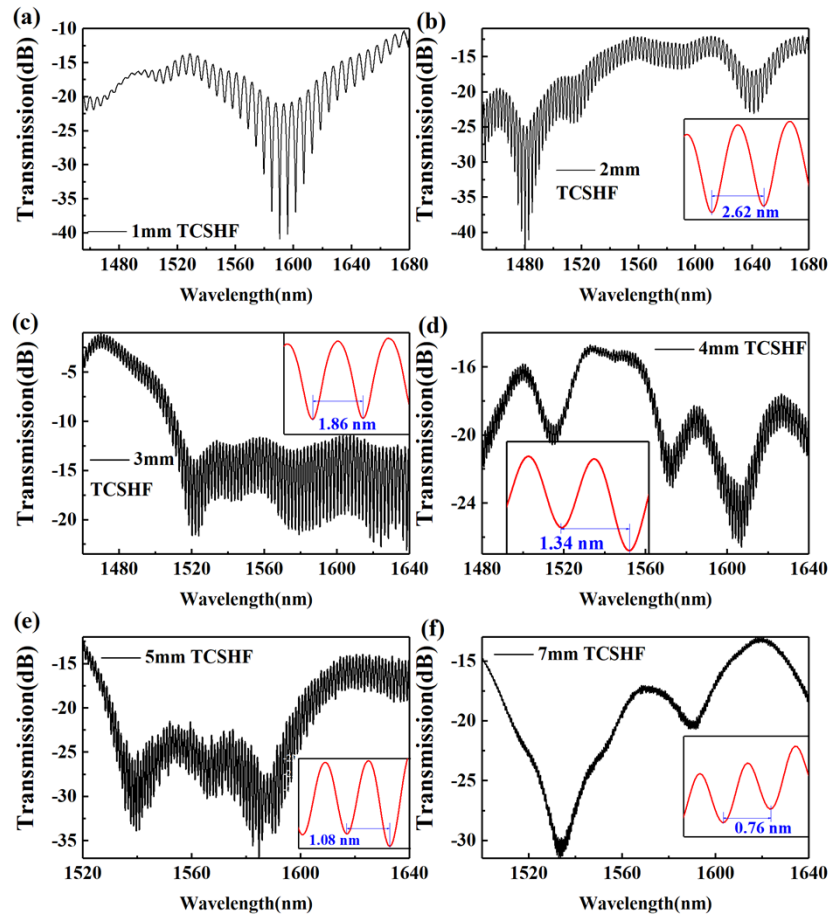
Fig. 5. The experimental transmission spectrums of the MZI structures under different lengths of TCSHF.
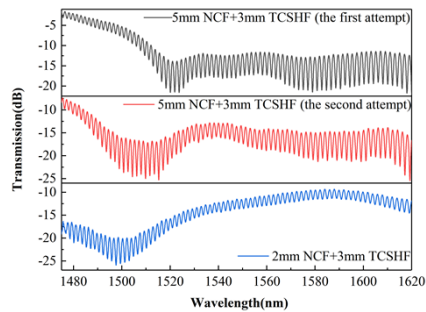

Fig. 6. The transmission spectrum of the MZI structure under different fabrication parameters.

3. Sensing principle

3.1. Mach-Zehnder interference

Concluded from the above analysis, the spectrum of the TCSHF sensor can be expressed as:

$$I = I_1 + I_2 + 2\sqrt{I_1 I_2} \cos \varphi \tag{2}$$

I_1 and I_2 are the light intensity of the beams in the core and air hole, respectively. The phase difference φ between the two light beams is related to the λ, Δn, and L.

$$\varphi = 2\pi \frac{\Delta n L}{\lambda}. \tag{3}$$

When the φ equals $(2m + 1)\,\pi$, the intensity of the transmission light will reach the minimum value. Then the dip wavelength can be expressed as:

$$\lambda = \frac{2}{2m + 1} \Delta n L. \tag{4}$$

If the sensor is used for temperature measurement, the relationship between λ and ΔT can be expressed as (5) based on the thermo-optic and thermal-expansion effects.

$$\frac{d\lambda}{dT} = \frac{2}{2m + 1} \left(\Delta n \frac{dL}{dT} + \frac{d\Delta n}{dT} L \right). \tag{5}$$

As for axial strain measurement, (4) can be transformed into (6) according to the elasto-optical and tensile deformation effects.

$$\frac{d\lambda}{d\varepsilon} = \frac{2}{2m + 1} \left(\Delta n \frac{dL}{d\varepsilon} + \frac{d\Delta n}{d\varepsilon} L \right). \tag{6}$$

3.2. Optical Vernier effect

The black line in Fig. 7 is the spectrum combining Sensor 1 and Sensor 2. To obtain the FSR of the spectrum resulting from the optical Vernier effect, a bandpass fast Fourier transform (FFT) filter is applied to the original spectrum. The result is shown by the orange line in Fig. 7. The threshold of the FFT filter is 0.24 Hz~0.76 Hz because the spatial frequencies of the two MZIs are around $1/1.86\,\text{nm} \approx 0.54\,\text{nm}^{-1}$ (Hz). Finally, the FSR envelope curve read from the orange line is ~55 nm, marked as FSR_v. The theoretical value of FSR_v is related to the FSRs of the two single interferometers, which can be calculated by the following equation.

$$FSR_v = \frac{FSR_1 FSR_2}{|FSR_1 - FSR_2|}. \tag{7}$$

After substituting 1.86 nm and 1.92 nm into (7), the theoretical value of FSR_v is obtained as 59.52 nm, which is close to the experimental value.

$$M = \frac{FSR_v}{FSR_1} = \frac{FSR_2}{|FSR_1 - FSR_2|}. \tag{8}$$

The magnification factor M of the cascaded structure compared to a single MZI can be calculated by Eq. (8). The theoretical value of M is 31.8.
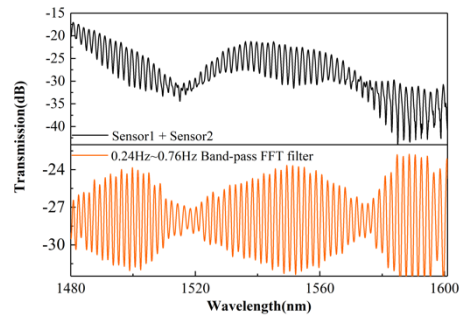
Fig. 7. The original transmission spectrum of the cascaded structure and the spectrum of it after the FFT filter.

4.   Experiments based on the MZI structure

4.1.   MZI for temperature sensing experiment

Figure 8 is the abridged general view of the temperature sensing system. The input light is provided by an ASE laser, and the output light is recorded by an optical spectrum analyzer (OSA, AQ6070D, Yokogawa). The temperature change is controlled by a Thermo−Electric Cooler (TEC, TLTP−TEC0510, Wuhan Talent Century Technology Co., Ltd). The function of the acrylic plate in this system is to ensure an even temperature distribution around the sensor. Figure 9(a) displays the spectrums of Sensor 1 under different temperatures from 30 °C to 65 °C with an interval of 5 °C. The inset in Fig. 9(a) is the enlarged view of the spectrums around 1550 nm. The spectrum of Sensor 1 shifts to a longer wavelength as the temperature increases. The specific relationship curves between temperature and dip wavelength are drawn in Fig. 9(b). As can be seen, the fitted curves could be expressed by linear equations. The slopes of the fitted curves represent the dip wavelength sensitives to temperature change. The sensitives of the three chosen dips are 34.19 pm/°C, 34.19 pm/°C, and 33.14 pm/°C, respectively. The values of the three sensitives only have a slight difference from each other, which means that the whole spectrum of Sensor 1 moves to the longer wavelength. Moreover, the temperature response of Sensor 2 is also tested to verify the repeatability of the proposed sensor, and the sensitivity is ∼34 pm/°C.
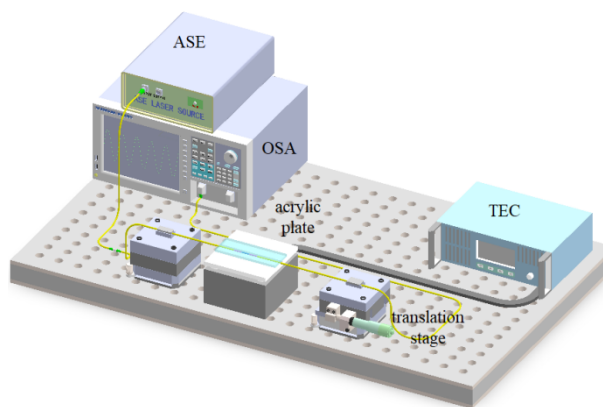

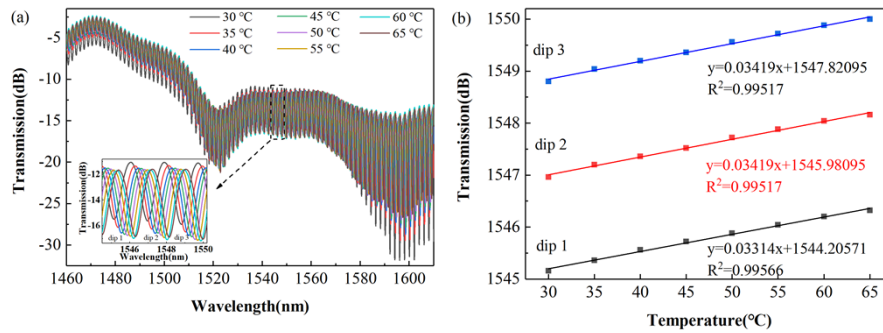**Fig. 8.** The experiment system for temperature measurement.

Fig. 9. (a) The spectrums of Sensor 1 at different temperatures; (b) The fitted curves of three dips between temperature change and dip wavelength shift.
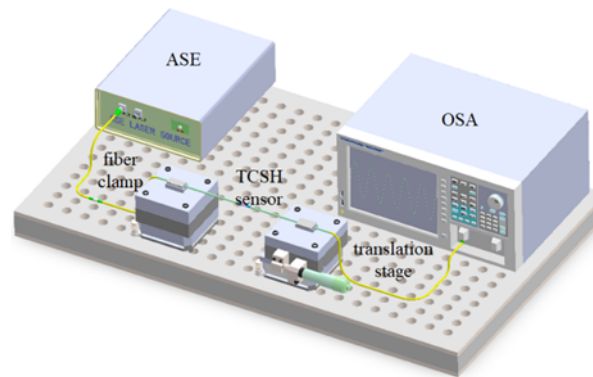

Fig. 10. The experiment system for axial strain measurement.

4.2. MZI for axial strain sensing experiment

Identical to the temperature sensing experiment, the two ends of the Sensor 1 are fixed on the translation stages by fiber clamps as shown in Fig. 10. The resolution of the translation stages is 0.01 mm, and the distance between the two translation stages is 20 cm. Thus, the axial strain change step value can be calculated as: 0.01/20 cm = 50 με. The spectrums of Sensor 1 under different axial strains in the range from 0 με to 1800 με are displayed in Fig. 10 with an interval of 200 με. From the illustration in Fig. 11(a), it can be easily observed that the dip wavelength shifts to the longer wavelength with the axial strain increasing.

Likewise, the sensitivities of the Sensor 1 to axial strain change at the three chosen dips can be calculated out: 0.59 pm/με, 0.59 pm/με, and 0.62 pm/με as shown in Fig. 11(b). The values of sensitivities are close to each other, which indicates that the spectrum of Sensor 1 moves to the longer wavelength as a whole with the axial strain increasing. The axial strain sensitivities of Sensor 2 are also tested, which are all around 0.6 pm/με.

4.3. Comparison between different structures of MZI

The sensors in Table 2 are all based on the symmetrical sandwich structure, as Fig. 12 shows. The function of the first and the last segments is like an optical coupler, which can enlarge or converge the mode field distribution. The middle segment can provide a transmission path for the MZ interference. As shown in the Table, the axial strain sensitivities of this sensor structure are generally lower than 2.5 pm/με, and the temperature sensitivities are less than 35 pm/°C. Though
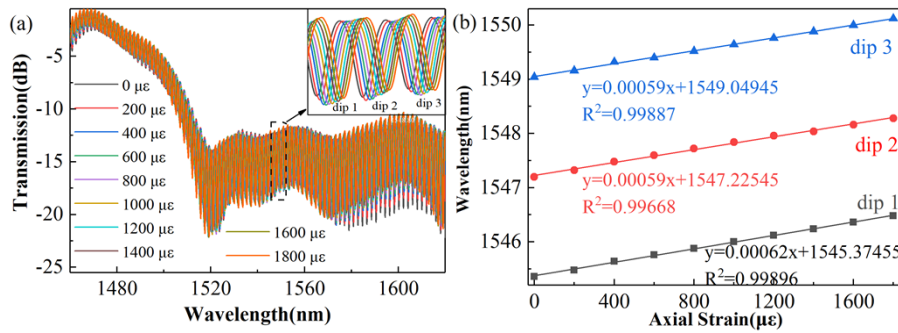
Fig. 11. (a) The spectrums of Sensor 1 under different axial strains; (b) The fitted curve between axial strain change and dip wavelength shift.

the preparation cost of this type of sensor structure is not very high, it is not practical in many measurement fields due to its low sensitivity.
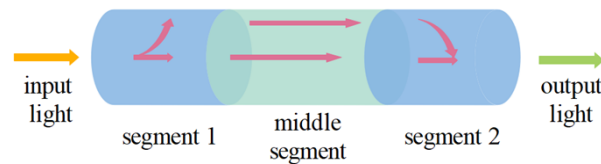

Fig. 12. The diagram of MZI with the sandwich structure.

Table 2. Comparison of the key parameters between the proposed sensor and the other types of MZI sensors

MZI structure	Strain sensitivity (pm/με)	Temperature sensitivity (pm/°C)	Ref.
MMF-TCF-MMF	-2.14	35.2	[31]
TCF-TF-TCF	-0.343	26.19	[32]
MMF-SCSHF-MMF	1.05	35.17	[33]
MMF-PCF-MMF	1.29	-	[34]
SMF-TCPCF-SMF	-0.31	6.68	[35]
NCF-HCF-NCF	0.652	30.92	[36]
NCF-TCSHF-NCF	0.6	34	This work

5. Experiments based on cascaded MZIs structure

It is noted that the fabrication repeatability of the proposed sensor is quite good compared with other structures. Benefitting from this, a cascaded structure based on the Optical Vernier Effect is designed and tested to improve the practicability and performance of the proposed sensor. In this paper, Sensor 1 and Sensor 2 are combined to realize Vinier Effect because of the slight difference between their FSRs. The characteristics of the structure spectrum have been discussed in Chapter 3.2.

5.1. Cascaded MZIs for temperature sensing experiment

As shown in Fig. 13, Sensor 1 is horizontally placed on the TEC heater, and Sensor 2 is fixed between two translation stages. In the experiment of temperature sensing, Sensor 1 is the sensing

element, while Sensor 2 serves as the reference. The spectrums of the cascaded structure in different environmental temperatures are shown in Fig. 14(a) with a step of 5 °C in the range from 30 °C to 70 °C. The vernier points around 1460 nm,1520 nm, and 1580 nm are marked as points A, B, and C, respectively. It can be observed that the marked points show a redshift when the temperature increases. Limited by the bandwidth of the light source, point A or point C cannot be captured when the environmental temperature is lower than 40 °C or higher than 50 °C. Figure 14(b) is the fitting curve of the relationship between temperature and the wavelength of gauge points. The fitted degrees are all above 0.99, which indicates that the spectrum of cascaded structures can respond linearly to temperature change. The sensitivities are 0.76 nm/°C at point A, 1.167 nm/°C at point B, and 1.588 nm/°C at point C.
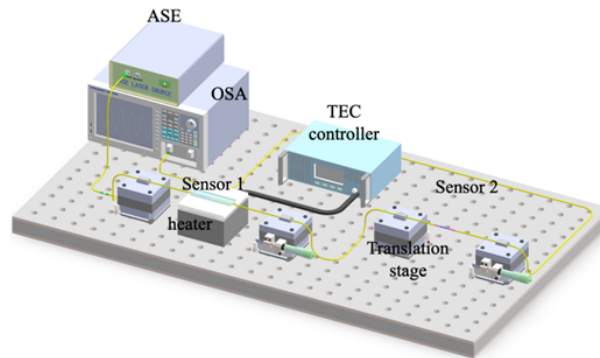

Fig. 13. The experiment system is designed for cascaded MZIs structure.
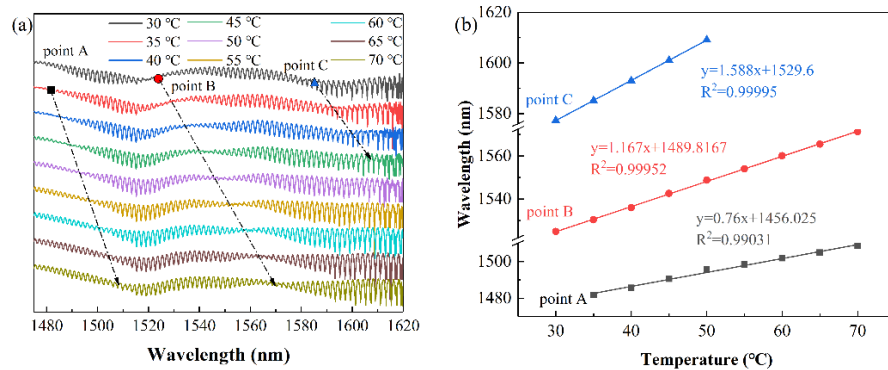

Fig. 14. (a) The spectrums of cascaded structure at different temperatures; (b) The fitted curve between temperature change and point wavelength.

Compared to the sensitivity of a single MZI, the sensitivity of the cascaded structure is much higher. The magnification factor M can be calculated as 1167/34≈34, which is in accord with the theoretical analysis in Chapter 3.

5.2.   *Cascaded MZIs for axial strain sensing experiment*

The axial strain measurement experiment is also conducted by the system displayed in Fig. 13. The only difference is that Sensor 2 serves as the sensing element while Sensor 1 serves as the reference element. According to the result shown in Fig. 15(a), the maximum range of axial strain measurement is 2000 με. The point B and C shift to the shorter wavelength with the axial strain

increasing. From the slopes and the fitted degree of the curves in Fig. 15(b), it can be concluded that the cascaded structure responds linearly to the axial strain fluctuation with sensitivities of -16.13 pm/µε at point B and -17.08 pm/µε at point A. The magnification factor M can also be calculated by 17.08/0.6≈28, which verifies the analysis result in Chapter 3.
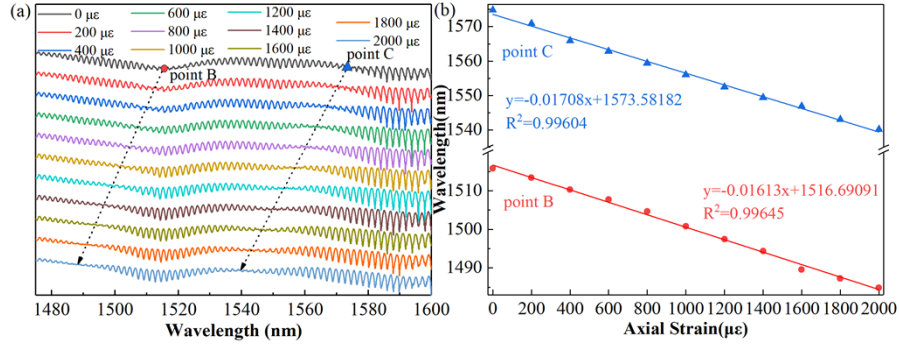

Fig. 15. (a) The spectrums of the cascaded structure under different axial strains; (b) The fitted curve between axial strain change and point wavelength shift.

5.3. *Cascaded MZIs for simultaneous measurement of axial strain and temperature*

Since the spectrum of the cascaded structure can separately respond linearly to the temperature or axial strain variation, the spectrum can also shift linearly if the temperature or axial strain changes simultaneously. In this case, points B and C are chosen as the monitoring points. Then, the wavelength offset value can be calculated by the following equation.

$$\begin{cases} \Delta\lambda_B = S_B^\varepsilon\Delta\varepsilon + S_B^T\Delta T \\ \Delta\lambda_C = S_C^\varepsilon\Delta\varepsilon + S_C^T\Delta T \end{cases}. \tag{9}$$

where the S^ε and S^T are the strain and temperature sensitivities, $\Delta\lambda$ is the value of the wavelength drift. $\Delta\varepsilon$ and ΔT are the value of the temperature and axial strain change, respectively. Equation (9) can be transformed to the matrix form as follow:

$$\begin{bmatrix} \Delta\lambda_B \\ \Delta\lambda_C \end{bmatrix} = \begin{bmatrix} S_B^\varepsilon & S_B^T \\ S_C^\varepsilon & S_B^T \end{bmatrix} \begin{bmatrix} \Delta\varepsilon \\ \Delta T \end{bmatrix}. \tag{10}$$

Then, the temperature and axial strain change value can be deduced according to the regulation of matrix operation.

$$\begin{bmatrix} \Delta\varepsilon \\ \Delta T \end{bmatrix} = \begin{bmatrix} S_B^\varepsilon & S_B^T \\ S_C^\varepsilon & S_B^T \end{bmatrix}^{-1} \begin{bmatrix} \Delta\lambda_B \\ \Delta\lambda_C \end{bmatrix}. \tag{11}$$

The resolution of the OSA used in this work is 0.1 nm. Thus, the theoretical error range of the $\Delta\varepsilon$ and ΔT can be calculated by (11), which are ±7.4 µε and ±0.017 °C.

Based on the above discussion result, the dual-parameter measurement is conducted by the system displayed in Fig. 13. In this experiment, Sensor 1 and Sensor 2 serve as temperature sensing element and strain sensing element, separately. The original axial strain added on Sensor 1 is 0 µε, and the original external temperature around Sensor 2 is 30 °C. The first step is changing the original axial strain added on Sensor 1 from 0 µε to 1000 µε. The second step is increasing
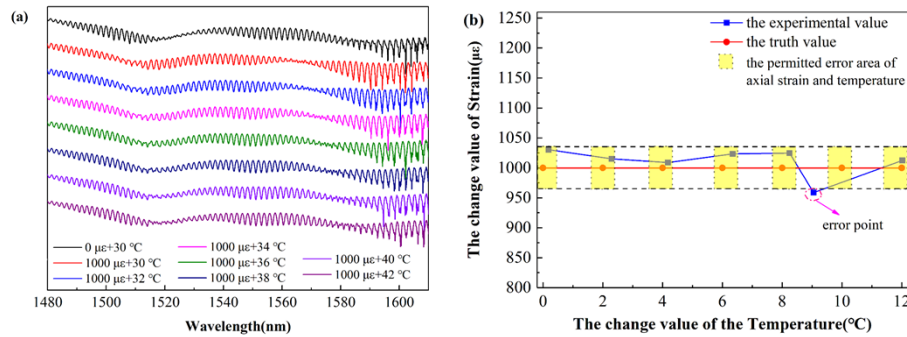
Fig. 16. (a) The spectrums of the cascaded structure under different axial strains and temperature; (b) The experimental values and the truth values for the dual parameter sensing experiment.

the external temperature around Sensor 2 from 30 °C to 42 °C with a step value of 2 °C. The spectrums under different states during the experiment process are shown in Fig. 16(a).

The blue points in Fig. 16(b) are the actual calculated values of every experimental state, and the red points are the truth values. Unfortunately, all experimental values are out of the permitted error range calculated by (11). The major error sources are the sensor itself and the experiment system. For the experiment system in this work, the resolutions of the translation stage and the TEC are the most error parameters for dual-parameter measurement because the wavelength drift value should be the multiple of the OSA resolution then the results will be more accurate. However, it is impossible to achieve such high resolution in the laboratory. The error from the sensor itself is related to the linearity of the sensor response, which can be deduced by improving the fabrication process. However, the proposed sensor can work well if the permitted error range of the $\Delta\varepsilon$ and ΔT are extended to ±40 με and ±0. 5 °C as the yellow areas shown in Fig. 16(b). Thus, the proposed sensor can be used for roughly measuring axial strain and temperature simultaneously.

5.4. Comparison with other sensors based on the optical Vernier effect

Table 3 summarizes the sensitivities for the different sensor configurations based on the Optical Vernier effect. Compared with other sensors, the proposed sensor has higher sensitivities and can simultaneously measure axial strain and temperature with an acceptable error limitation. The fabrication process of the proposed sensor is relatively simple because it is only related to the splicing fusion operation. The robustness of the sensor is also quite good. Since the diameter of all the fibers used is 125 μm, which sharply decreases the difficulty of encapsulation. Thus, the

Table 3. Comparison with other sensors' sensitivity

Sensor structure	Strain sensitivity (pm/με)	Temperature Sensitivity(pm/°C)	Dual-Parameter sensing	Ref.
FPIs	28.11	278.48	-	[37]
SIs	58	-1050	-	[38]
FPI + MZI	-	-107.2		[39]
MIs	-	143	-	[40]
HCF + SMF	18.36	-	-	[41]
Open FPI + HCF	-43.2	-27	-	[42]
MZIs	17.08	1167	Can work	This work

designed sensor has great potential for many application fields. For example, extensive building health monitoring in engineering, vital sign detection in the medical field, and so on.

6. Conclusion

This work proposes a sensor based on the optical Vernier effect for the dual-parameter measurement of temperature and axial strain. The main structure of the sensor is built up of two MZIs based on the symmetrical sandwich structure with similar structural parameters. The structure parameters are obtained from simulation experiments and the variable-controlled experiment. The splicing fusion parameters are also listed in detail, obtained from repeated experiments. In the experiment part, the sensing performance of the MZI is studied first. Each MZI can respond linearly to the axial strain change with a sensitivity of ~ 0.6 pm/με and temperature sensitivity of ~34 pm/°C. The sensitivities at this level are not competitive. Thus, two MZIs are combined to simplify the sensitivities about 34 times according to the optical Vernier effect principles. The proposed sensor has many other advantages, such as being fabricated easily, low cost, good robustness, and so on.

However, many downsides of the proposed sensor are also required to be investigated. For example, the accuracy of dual-parameter measurement should be improved. Besides, a simple interrogation system to process the response data of the sensor is an urgent need because it would help put the experimental results into the existing application system.

Disclosures. The authors declare no conflicts of interest

Data availability. Data underlying the results presented in this paper are not publicly available at this time but may be obtained from the authors upon reasonable request.

References

1. F. Tan, S. Chen, W. Lyu, Z. Liu, C. Yu, C. Lu, and H. Tam, "Non-invasive human vital signs are monitoring based on twin-core optical fiber sensors," Biomed. Opt. Express **10**(11), 5940–5952 (2019).
2. D. Barrera, I. Gasulla, and S. Sales, "Multipoint Two-Dimensional Curvature Optical Fiber Sensor Based on a Non-twisted Homogeneous Four-Core Fiber," J. Lightwave Technol. **33**(12), 2445–2450 (2015).
3. Y. N. Pang, B. Liu, J. Liu, S. P. Wan, T. Wu, X. He, J. Yuan, X. Zhou, K. Long, and Q. Wu, "Wearable Optical Fiber Sensor Based on a Bend Single mode-Multimode-Single mode Fiber Structure for Respiration Monitoring," IEEE Sens. J. **21**(4), 4610–4617 (2021).
4. W. W. Li, W. P. Chen, D. N. Wang, Z. K. Wang, and B. Xu, "Fiber inline Mach-Zehnder interferometer based on femtosecond laser inscribed waveguides," Opt. Lett. **42**(21), 4438–4441 (2017).
5. F. Tan, W. Lyu, S. Chen, Z. Liu, and C. Yu, "Contactless vital signs monitoring based on few-mode and multi-core fibers," Opto-Electron Adv. **3**(5), 190034 (2020).
6. P. Jiang, L. Ma, Z. Hu, and Y. Hu, "Low-Crosstalk and Polarization-Independent Inline Interferometric Fiber Sensor Array Based on Fiber Bragg Gratings," J. Lightwave Technol. **34**(18), 4232–4239 (2016).
7. C. Y. Lin, L. A. Wang, and G. W. Chern, "Corrugated long-period fiber gratings as strain, torsion, and bending sensors," J. Lightwave Technol. **19**(8), 1159–1168 (2001).
8. Y. Li, P. Lu, C. Zhang, W. Ni, D. Liu, and J. Zhang, "Sensing Characterization of Helical Long Period Fiber Grating Fabricated by a Double-Side CO2 Laser in Single-Mode Fiber," IEEE Photonics J. **11**(3), 1–8 (2019).
9. Z. Zhang, T. Guo, and B. Guan, "Reflective Fiber-Optic Refractometer Using Broadband Cladding Mode Coupling Mediated by a Tilted Fiber Bragg Grating and an In-Fiber Mirror," J. Lightwave Technol. **37**(11), 2815–2819 (2019).
10. Z. Tian and S. S. Yam, "In-Line Abrupt Taper Optical Fiber Mach–Zehnder Interferometric Strain Sensor," IEEE Photonics Technol. Lett. **21**(3), 161–163 (2009).
11. X. Hao, Z. Tong, W. Zhang, and Y. Cao, "A fiber laser temperature sensor based on SMF core-offset structure," Opt. Commun. **335**(15), 78–81 (2015).
12. R. Zhou, X. Qiao, R. Wang, F. Chen, and W. Ma, "An Optical Fiber Sensor Based on Lateral-Offset Spliced Seven-Core Fiber for Bending and Stretching Strain Measurement," IEEE Sens. J. **20**(11), 5915–5920 (2020).

13. R. Yang, Y. Yu, C. Chen, Y. Xue, X. Zhang, J. Guo, C. Wang, F. Zhu, B. Zhang, Q. Chen, and H. Sun, "S-Tapered Fiber Sensors for Highly Sensitive Measurement of Refractive Index and Axial Strain," J. Lightwave Technol. **30**(19), 3126–3132 (2012).

14. C. Zhang, P. Lu, H. Liao, W. Ni, X. Jiang, D. Liu, and J. Zhang, "Simultaneous Measurement of Axial Strain and Temperature Based on a Z-Shape Fiber Structure," IEEE Photonics J. **9**(4), 1–8 (2017).

15. S. H. Aref, R. Amezcua-Correa, J. P. Carvalho, O. Frazão, P. Caldas, J. L. Santos, F. M. Araújo, H. Latifi, F. Farahi, L. A. Ferreira, and J. C. Knight, "Modal interferometer based on hollow-core photonic crystal fiber for strain and temperature measurement," Opt. Express **17**(21), 18669–18675 (2009).

16. X. Dong, H. Y. Tam, and P. Shum, "Temperature-insensitive strain sensor with polarization-maintaining photonic crystal fiber based Sagnac interferometer," Appl. Phys. Lett. **90**(15), 1 (2007).

17. Zhengyong Liu, Ming-Leung Vincent Tse, Chuang Wu, Daru Chen, Chao Lu, and Hwa-Yaw Tam, "Intermodal coupling of super-modes in a twin-core photonic crystal fiber and its application as a pressure sensor," Opt. Express **20**(19), 21749–21757 (2012).

18. A. D. Gomes, H. Bartelt, and O. Frazão, "Optical Vernier Effect: Recent Advances and Developments," Laser Photonics Rev. **15**(7), 2000588 (2021).

19. Xiaohui Fang, Wu Zhang, Jiewen Li, Chunli Lin, Zhennan Chen, Meng Zhang, Shihong Huang, Dunke Lu, Minggui Wan, and Xiaozhong Qiu, "Signal processing assisted Vernier effect in a single interferometer for sensitivity magnification," Opt. Express **29**(8), 11570–11581 (2021).

20. Zhilin Xu, Qizhen Sun, Borui Li, Yiyang Luo, Wengao Lu, Deming Liu, Perry Ping Shum, and Lin Zhang, "Highly sensitive refractive index sensor based on cascaded microfiber knots with Vernier effect," Opt. Express **23**(5), 6662–6672 (2015).

21. Y. Liu, H. Chen, Q. Chen, B. Li, and S. Li, "Experimental study on dual-parameter sensing based on cascaded Sagnac interferometers with two PANDA fibers," J. Lightwave Technol. **40**(9), 3090–3097 (2022).

22. Y. Zhao, P. Wang, R. Lv, and X. Liu, "Highly Sensitive Airflow Sensor Based on Fabry–Perot Interferometer and Vernier Effect," J. Lightwave Technol. **34**(23), 5351–5356 (2016).

23. Yuanfang Zhao, Maolin Dai, Zhenmin Chen, Xuanyi Liu, M. S. Aruna Gandhi, Qian Li, and H. Y. Fu, "Ultrasensitive temperature sensor with Vernier-effect improved fiber Michelson interferometer," Opt. Express **29**(2), 1090–1101 (2021).

24. Hao Liao, Ping Lu, Xin Fu, Xinyue Jiang, Wenjun Ni, Deming Liu, and Jiangshan Zhang, "Sensitivity amplification of fiber-optic in-line Mach–Zehnder interferometer sensors with modified Vernier-effect," Opt. Express **25**(22), 26898–26909 (2017).

25. Yuqiang Yang, Yongguang Wang, Yuxin Zhao, Jiuxing Jiang, Xunjun He, Wenlong Yang, Zhihan Zhu, Wei Gao, and Linjun Li, "Sensitivity-enhanced temperature sensor by hybrid cascaded configuration of a Sagnac loop and an F-P cavity," Opt. Express **25**(26), 33290–33296 (2017).

26. T. Claes, W. Bogaerts, and P. Bienstman, "Experimental characterization of a silicon photonic biosensor consisting of two cascaded ring resonators based on the Vernier-effect and introduction of a curve fitting method for an improved detection limit," Opt. Express **18**(22), 22747–22761 (2010).

27. L. Liu, T. Ning, J. Zheng, L. Pei, J. Li, J. Cao, X. Gao, and C. Zhang, "High-sensitivity strain sensor implemented by hybrid cascaded interferometers and the Vernier effect," Opt. Laser Technol. **119**, 105591 (2019).

28. Xiaoshan Guo, Wenhao Ye, Chao Jiang, and Simei Sun, "High sensitivity gas pressure sensor based on two parallel-connected Fabry–Perot interferometers and Vernier effect," Meas. Sci. Technol. **32**(12), 125124 (2021).

29. Z. Wang, L. Huang, C. Liu, H. Wang, S. Sun, and D. Yang, "Sensitivity-Enhanced Fiber Temperature Sensor Based on Vernier Effect and Dual In-Line Mach–Zehnder Interferometers," IEEE Sensors J. **19**(18), 7983–7987 (2019).

30. M.Y. Xie, H.P. Gong, J. Zhang, C.L. Zhao, and X.Y. Dong, "Vernier effect of two cascaded in-fiber Mach-Zehnder interferometers based on a spherical-shaped structure," Appl. Opt. **58**(23), 6204–6210 (2019).

31. Xiaoli Zhao, Mingli Dong, Yumin Zhang, Fei Luo, Lianqing , and Zhu , "Simultaneous measurement of strain, temperature and refractive index based on a fiber Bragg grating and an in-line Mach–Zehnder interferometer," Opt. Commun. **435**, 61–67 (2019).

32. Wujun Zhang, Xuqiang Wu, Gang Zhang, Jinhui Shi, Cheng Zuo, Shasha Fang, Lei Gui, and Benli Yu, "Simultaneous measurement of refractive index and temperature or temperature and axial strain based on an inline Mach–Zehnder interferometer with TCF–TF–TCF structure," Appl. Opt. **60**(6), 1522–1528 (2021).

33. Y. Li, C. Yu, and P. Lu, "An Optical Fiber Sensor for Axial Strain, Curvature, and Temperature Measurement Based on Single-Core Six-Hole Optical Fiber," Sensors **22**(4), 1666 (2022).

34. Xinran Dong, Haifeng Du, Xiaoyan Sun, Zhi Luo, and Ji'an Duan, "A Novel Strain Sensor with Large Measurement Range Based on All Fiber Mach-Zehnder Interferometer," Sensors **18**(5), 1549 (2018).

35. K. K. Qureshi, Z. Liu, H. Tam, and M. Zia, "A strain sensor based on in-line fiber Mach–Zehnder interferometer in twin-core photonic crystal fiber," Opt. Commun. **309**(15), 68–70 (2013).

36. Yue Wu, Yuguang Yang, Wenxing Jin, Ya Shen, and Shuisheng Jian, "Compact Mach-Zehnder interferometer-based no-core fiber hollow-core fiber no-core fiber structure," Opt. Eng. **56**(3), 030501 (2017).

37. J. Deng and D. N. Wang, "Ultra-Sensitive Strain Sensor Based on Femtosecond Laser Inscribed In-Fiber Reflection Mirrors and Vernier Effect," J. Lightwave Technol. **37**(19), 4935–4939 (2019).

38. Shun Liu, Ping Lu, Enci Chen, Wenjun Ni, Deming Liu, Jiangshan Zhang, and Zhenggang Lian, "Vernier effect of fiber interferometer based on cascaded PANDA polarization maintaining fiber," Chin. Opt. Lett. **17**(8), 080601 (2019).

39. Yunbin Ying, Chunliu Zhao, Huaping Gong, Shiyan Shang, and Leyi Hou, "Demodulation method of Fabry-Perot sensor by cascading a traditional Mach-Zehnder interferometer," Opt. Laser Technol. **118**, 126–131 (2019).

40. S. Zhang, Y. Liu, H. Guo, A. Zhou, and L. Yuan, "Highly Sensitive Vector Curvature Sensor Based on Two Juxtaposed Fiber Michelson Interferometers with Vernier-Like Effect," IEEE Sens. J. **19**(6), 2148–2154 (2019).

41. Y. Wu, L. Xia, W. Li, and J. Xia, "Highly Sensitive Fabry–Perot Demodulation Based on Coarse Wavelength Sampling and Vernier Effect," IEEE Photonics Technol. Lett. **31**(6), 487–490 (2019).

42. Tong Nan, Bo Liu, Yongfeng Wu, Junfeng Wang, Yaya Mao, Lilong Zhao, Tingting Sun, and Jin Wang, "Ultrasensitive strain sensor based on Vernier- effect improved parallel structured fiber-optic Fabry-Perot interferometer," Opt. Express **27**(12), 17239–17250 (2019).